Pick, L., Korte, M. (2017): An annual proxy for the geomagnetic signal of magnetospheric currents on Earth based on observatory data from 1900–2010. - *Geophysical Journal International*, *211*, 2, pp. 1245—1258.

DOI: http://doi.org/10.1093/gji/ggx367

Geophysical Journal International

Geophys. J. Int. (2017) **211,** 1223–1236
Advance Access publication 2017 August 28
GJI Geomagnetism, rock magnetism and palaeomagnetism

doi: 10.1093/gji/ggx367

An annual proxy for the geomagnetic signal of magnetospheric currents on Earth based on observatory data from 1900–2010

Leonie J. L. Pick and Monika Korte

Helmholtz Centre Potsdam, GFZ German Research Centre for Geosciences, Behlertstrae 3a, Building K3, 14467 Potsdam, Germany.
E-mail: leonie.pick@gfz-potsdam.de

Accepted 2017 August 26. Received 2017 August 17; in original form 2017 April 28

SUMMARY

We introduce the Annual Magnetospheric Currents index as long-term proxy for the geomagnetic signal of magnetospheric currents on Earth valid within the time span 1900–2010. Similar to the widely used disturbance storm time and 'Ring Current' indices, it is based on geomagnetic observatory data, but provides a realistic absolute level and uncertainty estimates. Crucial aspects to this end are the revision of observatory crustal biases as well as the implementation of a Bayesian inversion accounting for uncertainties in the main field estimate, both required for the index derivation. The observatory choice is based on a minimization of index variance during a reference period spanning 1960–2010. The new index is capable of correcting observatory time series from large-scale external signals in a user-friendly manner. At present the index is only available as annual mean values. An extension to hourly values for the same time span is in progress.

Key words: Magnetic field variations through time; Satellite magnetics; Inverse theory; Statistical methods; Time-series analysis.

1 INTRODUCTION

The magnetic field of the Earth is highly irregular in space and time with relatively slowly varying internal sources in Earth's outer core, nearly static contributions from the upper lithosphere and more rapidly changing extraterrestrial sources. Over 90 per cent of this field is explained by a tilted axial dipole, that is produced by a self-sustaining geodynamo in the fluid core and changes on timescales of several months and beyond (secular variation, SV). This main field is overlain by the temporally stable crustal field from permanently magnetized rocks and comparably weak but highly variable induced fields in the electrically conducting parts of the crust and upper mantle. These originate as secondary contributions from the rapidly changing magnetic fields generated by electrical current systems in the ionosphere and magnetosphere.

Strategies to separate internal from external sources have been investigated since 1839 when Carl-Friedrich Gauss applied spherical harmonic analysis (SHA) to his observations of the magnetic vector field (details in Olsen *et al.* 2010). Since then the measurement network has steadily grown, with some observatories having recorded SV for up to ∼175 yr. In order to analyse the long-term time series with regard to core flow dynamics, all external contributions need to be eliminated from the measurements. The main influence that does not average out on SV timescales is the near-Earth signature of the large-scale magnetospheric field (e.g. Korte & Lesur 2012). This is commonly removed by fitting of a core field model rather than by directly cleaning the data as we propose here.

There are three current systems that regularly contribute to the magnetospheric signal recorded in observatory data. These are the ring current in the inner magnetosphere as well as the magnetopause current (Chapman-Ferraro current) and tail currents in the outer magnetosphere (details in e.g. chapters 10 and 13 of Wolf & McPherron 1995). They collectively produce a magnetic field at Earth that is globally southward directed and aligned with the dipole axis of the main field (Z_M axis, see Appendix A for details on coordinate systems). In particular it opposes the horizontal component of the core field at low to mid geomagnetic latitudes, especially when geomagnetic activity is high. During geomagnetic storms the disturbance field is dominated by an intensified ring current circling Earth in the equatorial plane at radial distances of 2–7 Earth radii (e.g. Daglis *et al.* 1999).

The Dst index (Sugiura 1964) combines the degree of main field depression measured at four mid-latitude observatories (HON, SJG, HER, and KAK) to characterize the global strength of the magnetospheric disturbance field. To enhance its use for geomagnetic field modelling, it was broken down into a direct external (Est) and an indirect induced (Ist) signal (Maus & Weidelt 2004; Olsen *et al.* 2005). Dst was reconstructed for the years 1932–2002 and corrected for semi-annual and seasonal variations, a normalization according to observatory latitude and an unequal weighting of the stations in a series of publications between 2005 and 2011 (see Mursula *et al.* 2011). The outcome of these changes is called Dcx index (Mursula & Karinen 2005) and is publicly available at the Dcx index server (see Appendix B for external data references). Furthermore

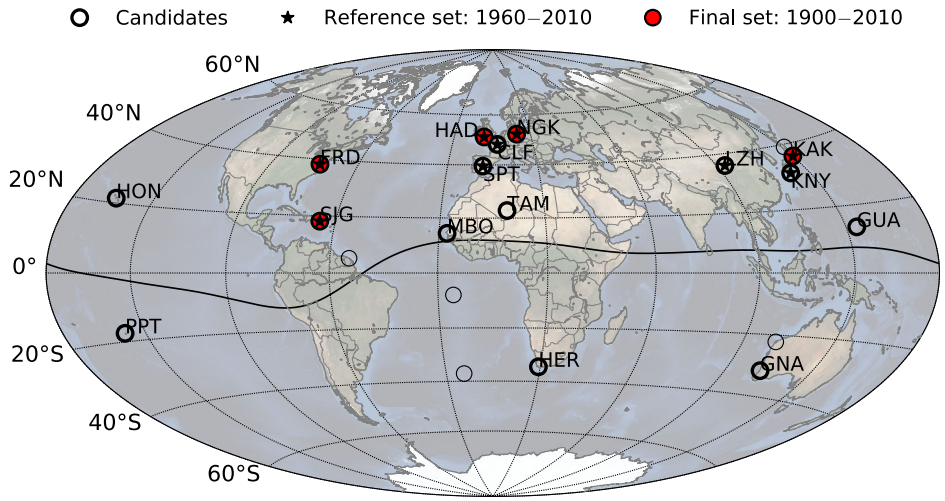

Figure 1. Locations of the 21 observatories used to derive the original RC index in relation to the geomagnetic equator (black line) from IGRF-12 for epoch 2015 (Thébault *et al.* 2015). 16 observatories are candidates for the AMC index (bold style, IAGA codes) and nine are found to be ideal during the reference period 1960–2010 (stars). Five observatories are finally chosen for the AMC index (red fillings).

the removal of the solar-quiet variation (Sq) was updated and the temporal resolution of the Dst increased to one minute (Gannon & Love 2011).

Despite all these improvements Dst still suffers from baseline instabilities (Olsen *et al.* 2005) that limit its adequacy for long-term studies. Therefore a new index called RC (Appendix B) was proposed as part of the CHAOS-4 geomagnetic field model (Olsen *et al.* 2014). It was originally derived from observatory hourly means (OHMs) at 21 globally distributed locations at low and mid geomagnetic latitudes ($-41^\circ \leq \theta'_M \leq 54^\circ$), excluding regions close to the geomagnetic equator that are affected by the equatorial electrojet. The OHMs were stripped of internal field contributions by subtracting a previous version of the CHAOS core field model. Second the resulting OHMs were averaged over quiet times (Kp $\leq 2^\circ$, $|\mathrm{dDst/d}t| \leq 2$ nT hr^{-1}) to approximate and subsequently remove lithospheric offsets at each site. The observatory residuals were then transformed into the spherical geomagnetic coordinate system (*mag*). At each universal time hour a SHA was performed on the residual horizontal components from night-side observatories (local time hours between 18 and 6). The RC index was then defined as the negative central external dipole term ($-q_1^0$), with the minus sign indicating a southward directed field at the dip equator. It can be split into a direct (RCE) and an induced (RCI) part following the same strategy as for the Dst index (see above).

According to a recent assessment by Lühr *et al.* (2017), RC is much more consistent with direct observations of the ring current effect made by the CHAMP satellite than Dst is. Thus it has replaced Dst in up-to-date geomagnetic field models such as the Swarm Initial Field Model (Olsen *et al.* 2015) as an hourly proxy for the magnetospheric field intensity. However, none of these indices assesses the absolute baseline of the quite-time magnetospheric field. Based on Magsat vector data the quiet-time magnetospheric field level was first estimated as 20 nT by Langel & Estes (1985a) and Langel & Estes (1985b). This first approximation was then specified using 9 yr of CHAMP data that revealed a stable quiet-time field of 13 nT with an additional variable part of up to 15 nT depending on the solar cycle phase (Lühr & Maus 2010). In the RC index derivation the crustal bias estimates include the average quiet-time magnetospheric field, that is consequently erroneously subtracted, causing a shift of RC to relatively less negative values.

In this study we propose a new index called AMC (*A*nnual *M*agnetospheric *C*urrents), that describes the large-scale magnetospheric field disturbances for 1900–2010 with improved absolute level and uncertainty estimates taking into account uncertainties in the used core field model. A simple extension of the RC index scheme to the past is not possible because many of the observatories used in the RC index derivation did not exist and the CHAOS core field model series is not valid before 1997.

We first give an overview of the involved observatory data (Section 2.1) and the geomagnetic field models (Section 2.2). We then explain the estimation of observatory crustal biases (Section 3.1) that are needed to form observatory residuals (Section 3.2) as the index basis. The actual derivation of the index is detailed in Section 3.3, followed by the presentation of results that are partitioned in a reference period 1960–2010 (Section 4.1) and the long-term period 1900–2010 (Section 4.2). The subsequent discussion covers the index' absolute level (Section 5.1), our reasoning regarding data choice (Section 5.2) and an example application (Section 5.3), before ending with conclusions (Section 6). Appendices A–D provide information on the coordinate systems, the data sources and the geomagnetic observatories as well as two extra figures. The AMC index is available in the Supporting Information.

2 DATA AND MODELS

2.1 Data

We base our study on observatory annual means (OAMs). They are available from the World Data Centre for Geomagnetism Edinburgh, hosted by the British Geological Survey (Appendix B), that also provides information on the corresponding locations, possible relocations and general measurement issues. Working with annual means has the main advantage that short-lived ionospheric disturbances, primarily the Sq daily variation, can be neglected. Although the Sq signal does not cancel in an annual average, its amplitude stays below 2 nT at a typical mid latitude observatory as Niemegk according to a study spanning the years 1960–2001 by Verbanac *et al.* (2007).

To identify a suitable database for our new AMC index, we consider the 21 observatories selected for the original RC index (Fig. 1).

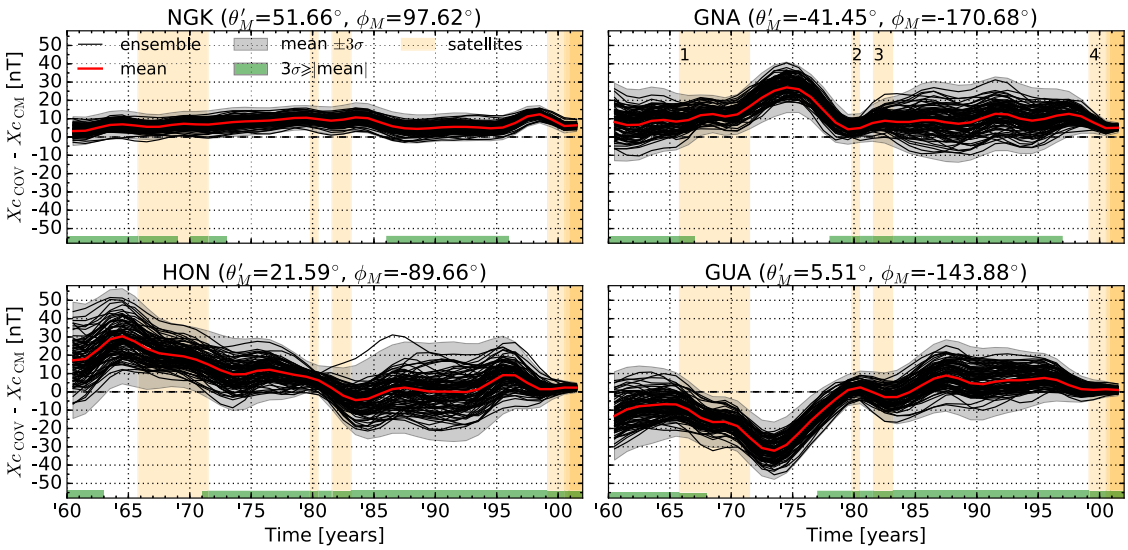

Figure 2. Yearly averaged differences between *Xc* components (core field, north, geodetic ned_d) of COV-OBS and CM4 up to d/o 14 calculated for 100 COV-OBS realizations (black) and their mean (red). The grey area marks the 99.73 per cent confidence interval. Green bars indicate years when COV-OBS's uncertainty envelope includes CM4. Satellite missions are (1) POGO series, (2) Magsat, (3) DE-2, (4) Ørsted, CHAMP & SAC-C successively. Observatory locations are given in geomagnetic coordinates (*mag*).

Due to the better data quality in the second half of the 20th century and the fact that some of the observatories were established not until the International Geophysical Year 1957–1958, we initially restrict our analysis to 16 candidates (details in Appendix C) covering the period 1960–2010 without gaps greater than 10 yr (see also Fig. 5). Based on a sensitivity analysis (Section 5.2) we identified a set of nine observatories as ideal choice for this period ('reference set'). Finally, five observatories from the reference set offer time series reaching back to the early 1900s and form the 'final set' for the AMC index (Section 4.2).

2.2 Models

Our requirements for modelled field contributions cannot be fulfilled by one model alone: First, we need a long-term model of the main field that preferably covers the complete observatory era (∼1840–present) to eliminate the core field influence from the OAMs. Second, we need a recent global field model including satellite data to estimate the large-scale external field at each observatory location. This is essential in order to ensure that our proxies for the high-degree crustal field contribution are free from external influences. Below, we briefly justify our decision in favour of the COV-OBS and GRIMM-3.2 field models (sources in Appendix B).

2.2.1 Long-term core field model

COV-OBS (Gillet *et al.* 2013) spans the period 1840–2010 and thereby is the only available model covering the current century and all years back to the beginning of observatory records. The ground-based data is essentially that used for the *gufm1* field model (Jackson *et al.* 2000), which is supplemented by satellite data from the missions marked in Fig. 2. It is a 'stochastic' field model that assumes a Gaussian prior probability distribution for the spherical harmonic (SH) coefficients of the geomagnetic potential that is expanded up to degree and order (d/o) 14. The dependence of the coefficients on time is parametrized by cubic B-splines with a knot spacing of 2 yr. COV-OBS calculates an ensemble solution of up to 100 members whose statistics equip the user with uncertainties, that are not provided by other core field models.

To demonstrate the usefulness of these uncertainties we compare COV-OBS to model CM4 (Sabaka *et al.* 2004), spanning 1960–2002, as a representative of other existing decadal field models. Following a 'comprehensive approach' CM4 estimates all internal and external sources of the geomagnetic field in a joint inversion of OHMs and satellite data. The difference in the northward core field component, *Xc*, from these two models is shown in Fig. 2 for four widely separated observatory locations from the reference set. While mean model differences (red) stay within ∼10 nT at European and East-Asian locations, for example, NGK, they climb to ∼20 nT at other observatories onshore, for example, GNA, and finally reach up to ∼30 nT at remote island-based stations, for example, HON and GUA. COV-OBS's confidence interval is given by three standard deviations, $\pm 3\sigma$, from the mean (grey band). It is reduced notably by the inclusion of vector field satellite data from Magsat and missions in the 2000s (orange bars 2 & 4). At most years (green horizontal bars), half the confidence interval is wider than the absolute mean model difference. This means that COV-OBS includes CM4 within its uncertainty, which seems reasonable overall.

2.2.2 Large-scale external field model

Seeking the most detailed description of external fields, the POMME (Maus *et al.* 2010, version six) model series would be a reasonable choice. It incorporates a dedicated magnetospheric field model (Lühr & Maus 2010) that requires five solar-terrestrial system parameters as input. Among them is the F10.7 index measuring solar radio flux per unit frequency at 10.7 cm wavelength. It complements Est in parametrizing the solar cycle dependence of the ring current. We use model version eight for testing, but any version from six to 11 could have been chosen as they all use the same magnetospheric field model.

The GRIMM-3.2 field model covers 2001–2010 and does not aim at describing distinct external field sources. Instead the whole range of vector CHAMP data at all local times is used to separate the

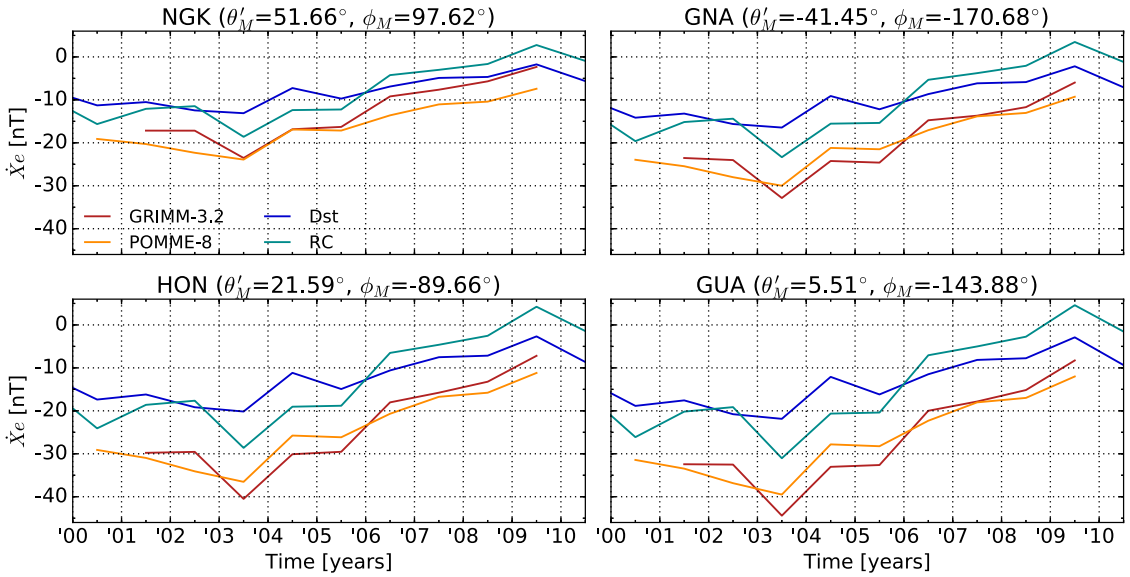

Figure 3. Yearly averaged $\dot{X}e$ components (external field, north, geocentric ned_c) of the large-scale external fields from GRIMM-3.2 (red) and POMME-8 (orange) in comparison with Dst (blue) and RC (green) indices. The decomposition of the indices into vector components is described at the end of Section 3.3. Observatory locations are given in geomagnetic coordinates (*mag*).

rapidly varying external field from the internal field. The external field parametrization closely follows that of the IGRF-12 candidate by Lesur *et al.* (2015) in which Est and IMF *By* control the rapidly varying part of the field. In the version we use, this is done by the SVMD index, a satellite-based modification (Kunagu *et al.* 2013) of the VMD index (Thomson & Lesur 2007).

Further options apart from these are the CHAOS (Finlay *et al.* 2016, version six) and CM (Sabaka *et al.* 2015, version five) model series. We reject both in order to preserve independence of the RC index, which is used in the latest versions of both these series. The Dst and RC indices provide additional possibilities of comparison to check the plausibility of the two considered external field models. Fig. 3 shows a common shape of the magnetospheric signal from models and indices at the same four locations as in Fig. 2. The signal's amplitude decreases with distance from the geomagnetic equator (GUA→NGK) and so does the offset between models and indices. Most importantly POMME-8 and GRIMM-3.2 are in remarkable agreement despite their different modelling techniques. This suggests that the models provide the correct absolute level of the magnetospheric signal as opposed to the indices (see Section 3.1). We favour GRIMM-3.2 as external field model given the simplicity of running the forward code compared to POMME-8.

3 METHODS

In order to extract the large-scale external signal from the observatory measurements the core field as well as local lithospheric anomalies have to be subtracted at each site. While the main field is given by the COV-OBS field model (Section 2.2.1), crustal offsets need to be estimated individually for each observatory. Below we describe the calculation of these biases followed by the calculation of measurement residuals, on the basis of which the AMC index is derived.

3.1 Observatory crustal biases

Time-dependent core field models are generally limited to SH degrees that include at most the large-scale lithospheric field (e.g. CM4 max. d/o 65). Crustal field models (e.g. Enhanced Magnetic Model EMM2017, Meyer *et al.* 2017) reach SH degrees up to 790 corresponding to a horizontal wavelength of 51 km. But even these dedicated models cannot resolve crustal anomalies in the direct vicinity of the observatories with amplitudes that may considerably exceed the external signal in question. The magnetic field contribution of such anomalies is commonly termed observatory crustal bias.

We assume the crustal biases to be constant over the period 1900–2010, thereby neglecting the possible variation of lithospheric anomalies that are induced. Between 1960 and 2002 the crustal field changes in the range $15 \leq$ d/o ≤ 19 are reported to be as weak as 0.06–0.12 nT yr^{-1} on average, not exceeding 1.3 nT yr^{-1} in South America at observatory Kourou (Thébault *et al.* 2009).

Temporal invariability of the crustal contribution allows us to base the calculation of biases on the GRIMM-3.2 field model (Section 2.2.2) although it only covers 9 yr out of the considered 110 yr period. Biases $\mathbf{Bb}_i$ are calculated for each observatory location $i = 1, \ldots, n$ by averaging the differences between the OAMs $\mathbf{Bo}_i(t)$ and core field $\mathbf{Bc}_i(t)$ (d/o ≤ 14) along with external field $\mathbf{Be}_i(t)$ (d/o ≤ 2) estimates from GRIMM-3.2:

$$\mathbf{Bb}_i = \frac{1}{9} \sum_{t=2001}^{2009} \mathbf{Bo}_i(t) - (\mathbf{Bc}_i(t) + \mathbf{Be}_i(t)) \qquad (1)$$

These biases (values listed in Appendix C) include contributions from the transitional spectrum range $15 \leq$ d/o ≤ 18. For these degrees GRIMM-3.2 yields a maximum root mean square core field intensity change of 0.08 nT/yr considering the locations of the 16 AMC candidate observatories (Fig. 1). This is negligible compared to the error introduced when subtracting the core field model and in line with the study cited above.

The advantage of the calculation method in eq. (1) is that we remove an estimation of the magnetospheric field $\mathbf{Be}_i(t)$ prior to averaging. This way the constant part of the external field signal is not included in the static lithospheric contribution $\mathbf{Bb}_i$, which is not achieved in the calculation of the Dst and RC indices. Both these indices underestimate the ring current effect by a constant amount

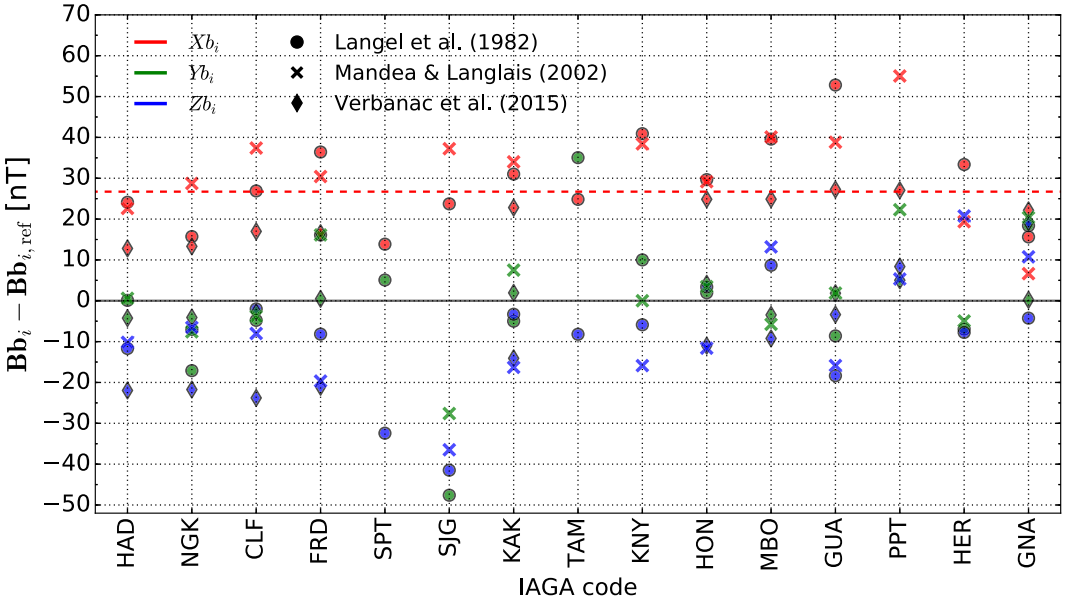

Figure 4. Differences between new biases (geodetic ned_d) and biases from three other studies (symbols). For these comparisons the effect of all jumps that occurred either after 1982 or after 2002 were removed (see also Verbanac *et al.* 2015). The values originally published by Langel *et al.* (1982) were taken from Gubbins & Bloxham (1985). Biases attributed to Mandea & Langlais (2002) are the means of their biases calculated either from Magsat or Ørsted data sets. The new *Xb* components (crustal bias, north, geodetic ned_d) are larger than those from the reference studies by 26.72 nT on average (red dashed line).

(see Fig. 3), that corresponds to the signal of the quiet-time background current and was erroneously attributed to the observatory offsets.

This effect is also evident when comparing our biases to biases from studies that do not consider the large-scale external field. Fig. 4 shows differences between our biases $\mathbf{Bb}_i$ and values from three other studies, namely Langel *et al.* (1982), Mandea & Langlais (2002) and Verbanac *et al.* (2015). While a detailed explanation of disagreements between these biases at specific locations is beyond the scope of our study, we want to highlight a systematic trend that is consistent across all studies. The components Xb_i (red) of our biases are larger than the reference biases by ∼27 nT on average (dashed red line). As the large-scale magnetospheric background field is reducing the main field's northward component, crustal biases calculated from uncorrected data will display lower amplitudes than those calculated from corrected data such as our offsets. On the basis of the new observatory biases we consequently expect the resulting AMC index to have the correct absolute level.

3.2 Observatory residuals

Observatory residuals $\mathbf{B}_i(t)$ can now be estimated by subtracting the modelled core field $\mathbf{Bc}_i(t)$ (COV-OBS, d/o ≤ 14) together with the corresponding crustal biases $\mathbf{Bb}_i$ (eq. 1) from the OAMs at each station $i = 1, \ldots, n$ and for each year in the long-term period:

$$\mathbf{B}_i(t) = \mathbf{Bo}_i(t) - \mathbf{Bc}_i(t) - \mathbf{Bb}_i. \tag{2}$$

The residual vectors $\mathbf{B}_i(t)$ should then essentially consist of the external magnetospheric signal. The major part of this signal can be represented by only one vector component, $Z_{M,i}(t)$, that points northward along the main field's dipole axis. Starting from local geodetic (i.e. spheroidal) coordinates (ned_d), $\mathbf{B}_i(t)$ is adjusted to geocentric (i.e. spherical) coordinates (ned_c or seu_c) before being transformed into the Cartesian geographic (GEO) and geomagnetic (MAG: X_M, Y_M, Z_M) systems. The position and field vectors are finally converted to a spherical system (*mag*: $B_{\theta,M}$, $B_{\phi,M}$, $B_{r,M}$) ready for further analysis:

$$\mathbf{B}_{ned_d} \underbrace{\overset{1}{\rightarrow}}_{\mathrm{WGS-84}} \left[\mathbf{B}_{ned_c}, \mathbf{B}_{seu_c}\right] \overset{2}{\rightarrow} \mathbf{B}_{\mathrm{GEO}} \underbrace{\overset{3}{\rightarrow}}_{\mathrm{IGRF-12}} \mathbf{B}_{\mathrm{MAG}} \overset{4}{\rightarrow} \mathbf{B}_{mag}. \tag{3}$$

Refer to Appendix A for the nomenclature and to Hapgood (1992) for coordinate transformations.

3.3 Index derivation

The pending task is to transfer the individual observatory residuals into a time-dependent index with global validity. The simplest option is to consider an average external signal $\overline{Z_M}(t)$ as the arithmetic mean of residual components $Z_{M,i}(t)$ from all contributing observatories at each year. This requires the residuals to be entirely independent from the observatory location, which is analysed in Section 4.1. A more sophisticated option is to apply a year-by-year SHA to the residuals $\mathbf{B}_{mag}$, called $\mathbf{B}$ hereafter, in which case their dependency on location (θ_M, ϕ_M, r—geomagnetic colatitude, longitude, radius) is considered. The observatory residuals are taken to be the negative gradient of a scalar potential, V_e, that fulfils Laplace's equation:

$$\mathbf{B} = -\nabla V_e\,, \qquad \nabla^2 V_e = 0. \tag{4}$$

We consider an external large-scale geomagnetic potential whose expansion into spherical harmonics is truncated at degree one:

$$V_e(\theta_M, \phi_M, r) = a \sum_{m=0}^{1} \left(\frac{r}{a}\right) \left[q_1^m \cos\left(m \cdot \phi_M\right) + s_1^m \sin\left(m \cdot \phi_M\right)\right] P_1^m\left(\cos\left(\theta_M\right)\right). \tag{5}$$

The potential increases with radial distance from Earth's centre (r) towards the source region in the magnetosphere and is evaluated at a mean radius of $a = 6371$ km. Above, $\{{}^{q}_{s}\}_1^m$ denote the three Gauss coefficients of degree one and order m and P_1^m are the Schmidt

semi-normalized Associated Legendre Polynomials (Schmidt 1917) including the Condon–Shortley phase factor.

The combined observatory residual vector $\mathbf{B}$ ($k = 1, \ldots, N_D = 3 \cdot n$ entries) contains three vector components from each of the n observatories. It is connected to the vector of Gauss coefficients $\mathbf{x}$ (3 entries) via the ($N_D \times 3$) matrix $\mathbf{A}$:

$$\underbrace{\begin{pmatrix} B_{\theta 1} \\ B_{\phi 1} \\ B_{r 1} \\ \vdots \\ B_{rn} \end{pmatrix}}_{\mathbf{B}} = \underbrace{\begin{pmatrix} \sin(\theta_1) & \cos(\phi_1)\cos(\theta_1) & \sin(\phi_1)\cos(\theta_1) \\ 0 & -\sin(\phi_1) & \cos(\phi_1) \\ -\cos(\theta_1) & \cos(\phi_1)\sin(\theta_1) & \sin(\phi_1)\sin(\theta_1) \\ \vdots & \vdots & \vdots \\ -\cos(\theta_n) & \cos(\phi_n)\sin(\theta_n) & \sin(\phi_n)\sin(\theta_n) \end{pmatrix}}_{\mathbf{A}} \cdot \underbrace{\begin{pmatrix} q_1^0 \\ q_1^1 \\ s_1^1 \end{pmatrix}}_{\mathbf{x}} \tag{6}$$

The inversion of this linear forward problem for the coefficients $\mathbf{x}$ should consider the propagation of errors from $\mathbf{B}$ that are mainly due to uncertainties in the COV-OBS main field results (Section 2.2.1). We therefore adopt a Bayesian approach (method detailed in e.g. Gelman *et al.* 2014) in which we assume an uninformative prior probability density function (PDF), $\rho(\mathbf{x}) = 1$, and a likelihood distribution $\rho(\mathbf{B}|\mathbf{x})$ of multivariate Gaussian type $\mathbf{B} \propto \mathcal{N}(\boldsymbol{\mu}, \boldsymbol{\Sigma})$. The latter describes the spread of the residuals, $\mathbf{B}$, around reality, modelled as $\mathbf{A} \cdot \mathbf{x}$, according to uncertainties from COV-OBS. The residual mean, $\boldsymbol{\mu}$ (N_D entries), and covariance matrix, $\boldsymbol{\Sigma}$ ($N_D \times N_D$), are calculated from the COV-OBS main field ensemble comprising $j = 1, \ldots, N_E = 100$ residual vectors, $\mathbf{B}_j$, per time step. We neglect the off-diagonal elements in $\boldsymbol{\Sigma}$ because errors in the components of $\mathbf{B}$ and among the observatories are assumed to be uncorrelated. This way $\boldsymbol{\Sigma}$ is diagonal and contains the squares of standard deviations σ:

$$\mu_k = \frac{1}{N_E} \sum_{j=1}^{N_E} B_{jk}$$

$$\Sigma_{k,k} = {\sigma_k}^2 = \frac{1}{N_E - 1} \sum_{j=1}^{N_E} \left(B_{jk} - \mu_k\right)^2 . \tag{7}$$

The posterior PDF $\rho(\mathbf{x}|\mathbf{B})$ is Gaussian as well with $\mathbf{x} \propto \mathcal{N}(\boldsymbol{\mu}_\mathbf{x}, \boldsymbol{\Sigma}_\mathbf{x})$, so its maximization yields the mean of the Gauss coefficients:

$$\boldsymbol{\mu}_\mathbf{x} = \left(\mathbf{A}^T \boldsymbol{\Sigma}^{-1} \mathbf{A}\right)^{-1} \mathbf{A}^T \boldsymbol{\Sigma}^{-1} \boldsymbol{\mu}. \tag{8}$$

The posterior covariance matrix, $\boldsymbol{\Sigma}_\mathbf{x}$ (3×3 entries), is symmetric with negligible off-diagonal elements. It contains the variances of the coefficients on the diagonal

$$\boldsymbol{\Sigma}_\mathbf{x} = \left(\mathbf{A}^T \boldsymbol{\Sigma}^{-1} \mathbf{A}\right)^{-1} = \begin{pmatrix} \sigma_\mathrm{x}(q_1^0)^2 & \bullet & \circ \\ \bullet & \sigma_\mathrm{x}(q_1^1)^2 & \diamond \\ \circ & \diamond & \sigma_\mathrm{x}(s_1^1)^2 \end{pmatrix}. \tag{9}$$

Because the strongest magnetospheric signal is aligned with the dipole axis, we define the AMC index as

$$\mathrm{AMC} := -q_1^0 \propto \mathcal{N}\left(-\mu_\mathrm{x}(q_1^0), \sigma_\mathrm{x}(q_1^0)^2\right). \tag{10}$$

The negative sign makes our index definition comparable with those of the Dst and RC indices as southward disturbances that are given with respect to the Z_M axis pointing northward along the dipole axis. In further agreement with Dst and RC, the AMC index contains the direct external signal as well as the signal that is induced in the conductive upper layers of Earth's interior. A separation of these two parts is possible following the strategy of Maus & Weidelt (2004) or Olsen *et al.* (2005), but is not necessary for our purposes at this stage.

The AMC index can be used to correct observatory data (Bo_θ, Bo_ϕ, Bo_r) for large-scale external disturbances. To do so, AMC intensity needs to be split in three vector components (AMC_θ, AMC_ϕ, AMC_r) according to the following steps:

(1) Calculate the position of the geomagnetic dipole ($\theta_P{}'$, ϕ_P) and accordingly convert the geocentric observatory position (θ_c, ϕ, r) to geomagnetic coordinates (θ_M, ϕ_M, r). Colatitudes are named θ whereas latitudes are labelled θ'.

(2) Determine the angle (D) between geographic and geomagnetic north:

$$D = s \cdot \cos^{-1}\left(\frac{\sin(\theta_P{}') - \sin(\theta_c{}')\cos(\theta_M)}{\cos(\theta_c{}')\sin(\theta_M)}\right),$$

$$s = \begin{cases} -1 & \text{for } 0^\circ \leqslant \phi - \phi_P \leqslant 180^\circ \\ 1 & \text{otherwise} \end{cases} \tag{11}$$

(3) The index components are:

$$\begin{aligned} \mathrm{AMC}_r &= \cos(\theta_M) \cdot \mathrm{AMC} \\ \mathrm{AMC}_H &= -\sin(\theta_M) \cdot \mathrm{AMC} \\ \mathrm{AMC}_\theta &= \cos(D) \cdot \mathrm{AMC_H} \\ \mathrm{AMC}_\phi &= -\sin(D) \cdot \mathrm{AMC_H} \end{aligned} \tag{12}$$

The corrected data is obtained by subtracting the appropriate index component in eq. (12) from the corresponding observatory measurement.

4 RESULTS

We begin with an analysis of the annual residual mean ($\boldsymbol{\mu}$, eq. 7) time series from the 16 observatories in the reference set (Fig. 1), that leads the way to the presentation of the AMC index.

4.1 Reference period: 1960–2010

Fig. 5 (top) shows residual mean components, Z_M, that are sorted by the geomagnetic latitudes of the corresponding observatories from north (top) to south (bottom). The vertical stripes illustrate a pronounced similarity of the residuals at all sites. There is no distinct dependence on location.

The degree of the signal's global uniformity improves with time. The middle panel of Fig. 5 shows the scatter in amplitude (error bars) around the average external signal $\overline{Z_M}(t)$ from the 16 AMC candidate stations (red IAGA codes). For the period 1999–2010, the mean scatter is only 49 per cent of what it was in the previous period 1960–1998. We attribute this reduction to the fact that COV-OBS profits from continuous vector satellite data since the turn of the century (Fig. 2). Note that the scatter in amplitude would have been larger by ∼11 nT on average, if we had used CM4 (57 nT) instead of COV-OBS (46 nT) as main field model.

The variations of the average external signal show clear resemblances to other geomagnetic indices shown in Fig. 5 (bottom, sources in Appendix B). Altogether the extracted signal is consistent with the globally southward directed (negative Z_M values) magnetic field signature of the magnetospheric current system in response to the solar cycle. Low-frequency variations thus respond to the F10.7 index with some time-lag that cannot be estimated reasonably based on annual means but should be about 20 months

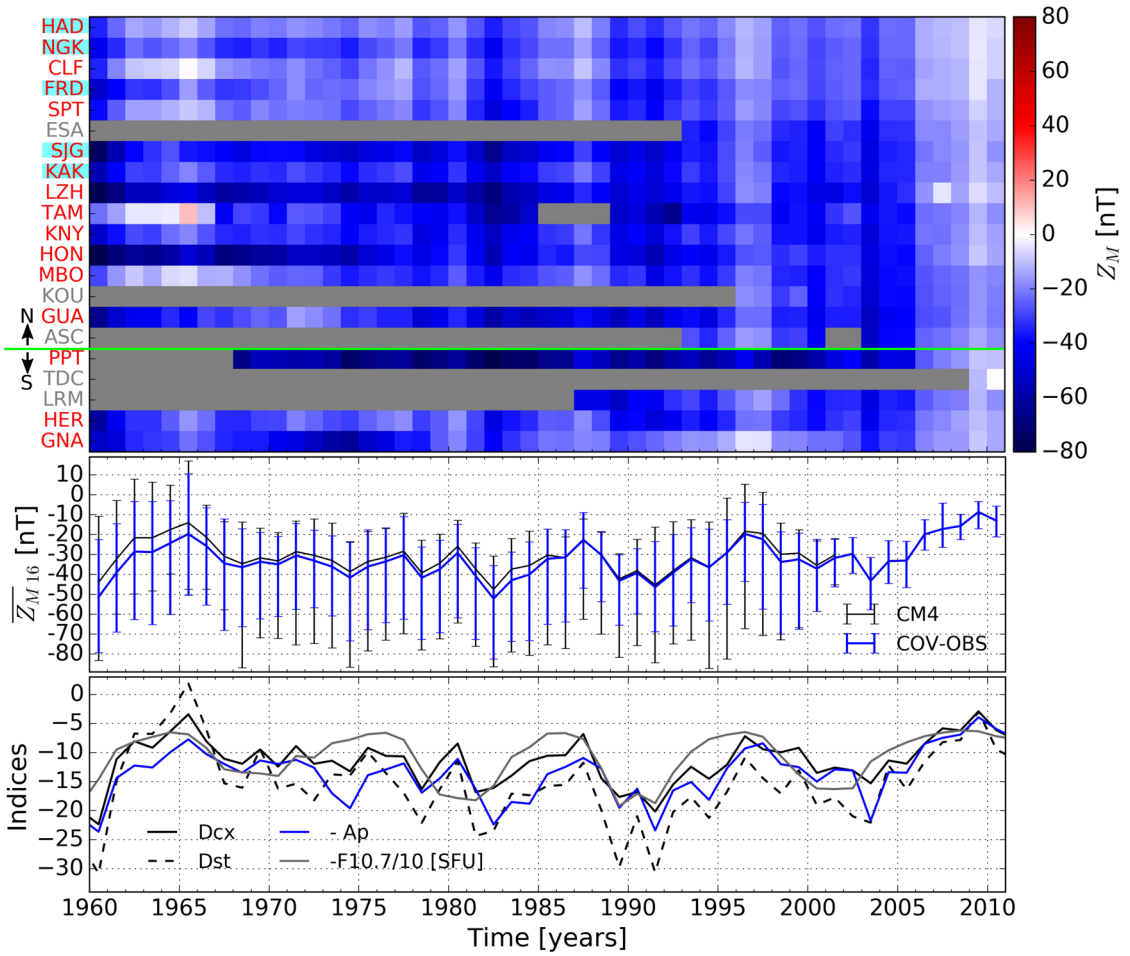

Figure 5. Top: observatory residuals Z_M (north, geomagnetic MAG) from 21 observatories (Fig. 1) sorted by geomagnetic latitude from north (top) to south (bottom). The green horizontal line separates observatories north and south of the geomagnetic equator. Missing annual means are marked in grey. IAGA codes of the 16 AMC candidate observatories (red) and the five final observatories (cyan) are highlighted. Middle: mean external signal $\overline{Z_M}$ from AMC candidate stations calculated using either COV-OBS or CM4. Error bars indicate the maximum spread from the mean. Bottom: annual means of the Dcx, Dst, Ap (negative) and absolute solar flux index F10.7 (negative & scaled).

according to (Lühr & Maus 2010). Under solar minimum conditions the signal is expected to be particularly small, albeit still negative. An extremely quiet year was 1965 when the only positive residual is calculated at TAM (11 nT). If not a data issue, this could be caused by a non-vanishing contribution from ionospheric currents, too small to be recognized at other times. The exceptional character of that year is also expressed by the uniquely positive Dst value (dashed line). This was corrected for the revised Dcx index (black line) by Karinen & Mursula (2005). However, our average external signal (middle panel, blue line) correlates better with the Ap index (Pearson coefficient $r = -0.94$) than with the Dcx index ($r = 0.87$).

In the top panel of Fig. 6(a) the average external signal, $\overline{Z_M}(t)$ (dashed line), is compared to the AMC index (solid line) calculated either from the reference set of nine observatories (green) or the final set of five observatories (blue). For recent years, the temporal variability of all these results agrees with that of the annual RC index (black). Likewise it agrees with an average over external field estimates from GRIMM-3.2 (Section 2.2.2) for the locations of observatories in the final set (red). As expected (Section 3.1) there is an offset between the RC index and the final AMC index, which amounts to -12.2 ± 1.2 nT and is discussed further in Section 5.1.

The error bars of the two AMCs overlap at all times within the 50 yr period (orange shaded region), except in the year 2003. The corresponding average external signals tend to lie at comparable or more negative values than the AMCs and fall within the overlapping region at most years. However, they are notably cutting across the AMCs during the years 1979–1980 and 1999–2010, clearly surpassing the common uncertainty boundaries in the latter case.

This behaviour is linked to the variances of the core field estimates from COV-OBS, that are located on the diagonal of the covariance matrix $\mathbf{\Sigma}$ (eq. 7). The normalized trace of $\mathbf{\Sigma}$ measures the spatially averaged core field uncertainty and is shown in the bottom panel of Fig. 6(a) for both location sets. When the core field uncertainty decreases, so does the uncertainty of the AMC index. This relation scales with the number of contributing observatories, n, such that a gain in information, that is, a greater n, results in smaller AMC uncertainties. The efficiency of the uncertainty reduction depends on the specific choice of observatories with regard to the global distribution of core field uncertainty. If satellite data is available to COV-OBS, for example, in years 1980 and 2010 (Fig. 2), differences in core field uncertainty amongst mid latitude observatories are marginal, so that their distribution is irrelevant to the AMC index. However, for all other times, for example, year 1990, COV-OBS's core field uncertainties are globally heterogeneous, favouring observatories in regions with dense coverage, especially from Europe and Japan. Maps showing the core field uncertainty from

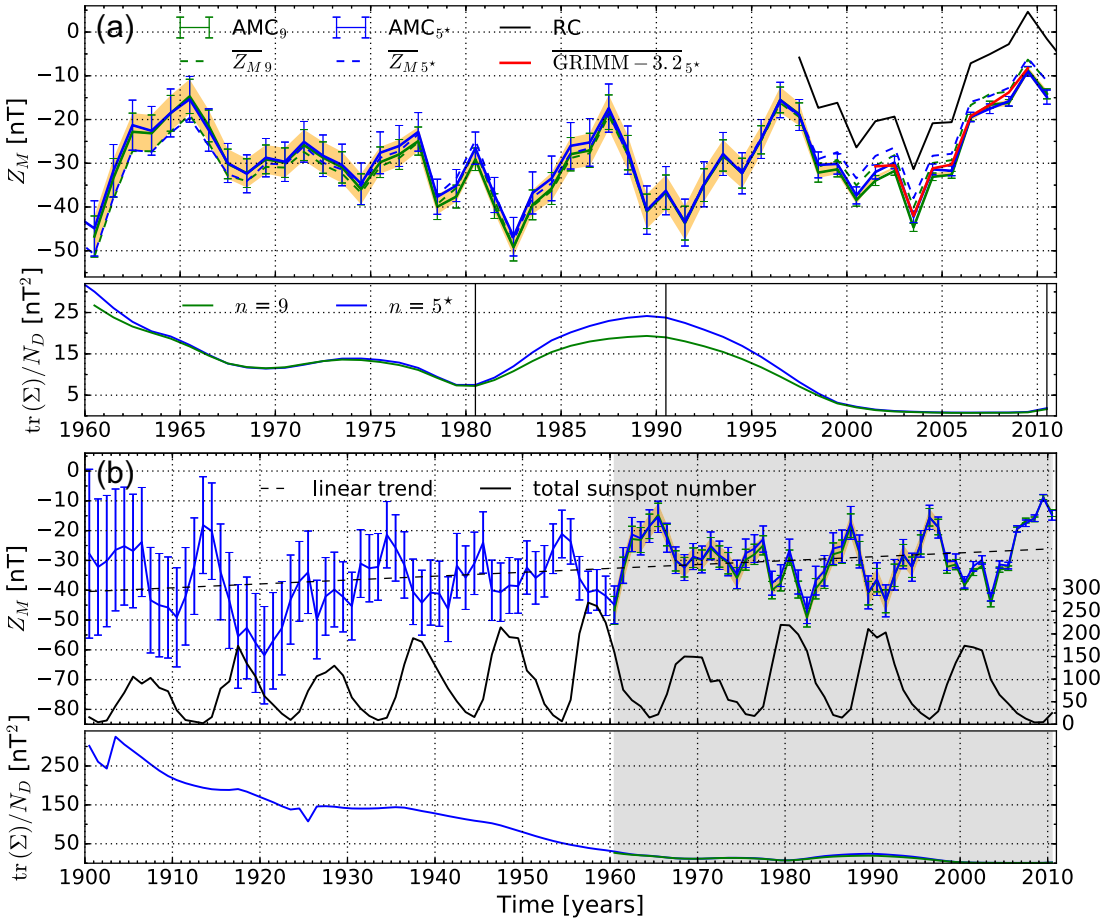

Figure 6. (a) Top: mean external signal $\overline{Z_M}$ (dashed line) and AMC index with ∼99.73 per cent confidence (solid line with error bars) for the reference set (green) and the final set (blue) of observatories (Fig. 1). The times when the error bars overlap are shaded in orange. Also shown are the RC index (black) and external field estimates from GRIMM-3.2 averaged over the locations of stations in the final set (red). Bottom: trace of the COV-OBS covariance matrix $\boldsymbol{\Sigma}$ normalized by the number of data points N_D from the same two data sets. Vertical black lines indicate years with distinct global patterns of COV-OBS main field uncertainties that are presented in Appendix D, Fig. D1. (b) Grey shaded region is the same as in panel (a) but here the complete time span 1900–2010 is shown with the total sunspot number for comparison (right ordinate). Estimated linear trend for the AMC index is 0.13 nT yr^{-1} (dashed black line).

COV-OBS for the mentioned years can be found in Appendix D, Fig. D1.

4.2 Long-term period: 1900–2010

The final AMC index cannot be calculated from the OAMs in the reference set (Fig. 1), because three out of the nine observatories (KNY, LZH, and SPT) do not provide long enough time series. Additionally, special care has to be taken of observatory relocations. Observatory residuals in the style of Fig. 5 with marked relocations can be found in Appendix D, Fig. D2 for the long-term period. The figure indicates that there are serious issues with the OAMs from Val Joyeux (VAL), the predecessor of CLF, persisting roughly from 1906–1931. The complete time series was therefore discarded which led to the final data set.

Based on core field estimations from COV-OBS we found that the secular variations at subsequent locations of an observatory can differ substantially. In particular, discrepancies are large between Greenwich (GRW) and Hartland (HAD), which are separated by more than 300 km. We therefore calculated observatory residuals individually for each location and reassembled the sections by applying an offset accounting for the different observatory biases. This offset is estimated as the difference between the jump modelled with COV-OBS (not including biases) and the jump in the OAMs (including biases) at the year of the relocation. Data jumps are documented in the BGS annual records, but in the case of POT→SED→NGK the POT and SED values were already adjusted to the NGK location and jump values had to be taken from Bock (1950).

The resulting long-term AMC index is shown in Fig. 6(b) including the two panels from Fig. 6(a) in the grey shaded region. The increase of AMC uncertainties at earlier times is expected, as is the fact that local minima closely follow peaks in the total sunspot number (black, right ordinate). The AMC shows a small positive trend over the 110 yr period amounting to ∼0.13 nT yr^{-1}, that is not matched by the solar activity evolution. In view of the large uncertainties we cannot confirm this trend to be physically real at this point.

5 DISCUSSION

In this section we assess the presented AMC index in several regards. First, we concentrate on the absolute level of the index and second discuss our observatory choice as constrained by the index variance. Lastly, we apply the AMC index to observatory measurements from the reference period and illustrate implied scientific opportunities.

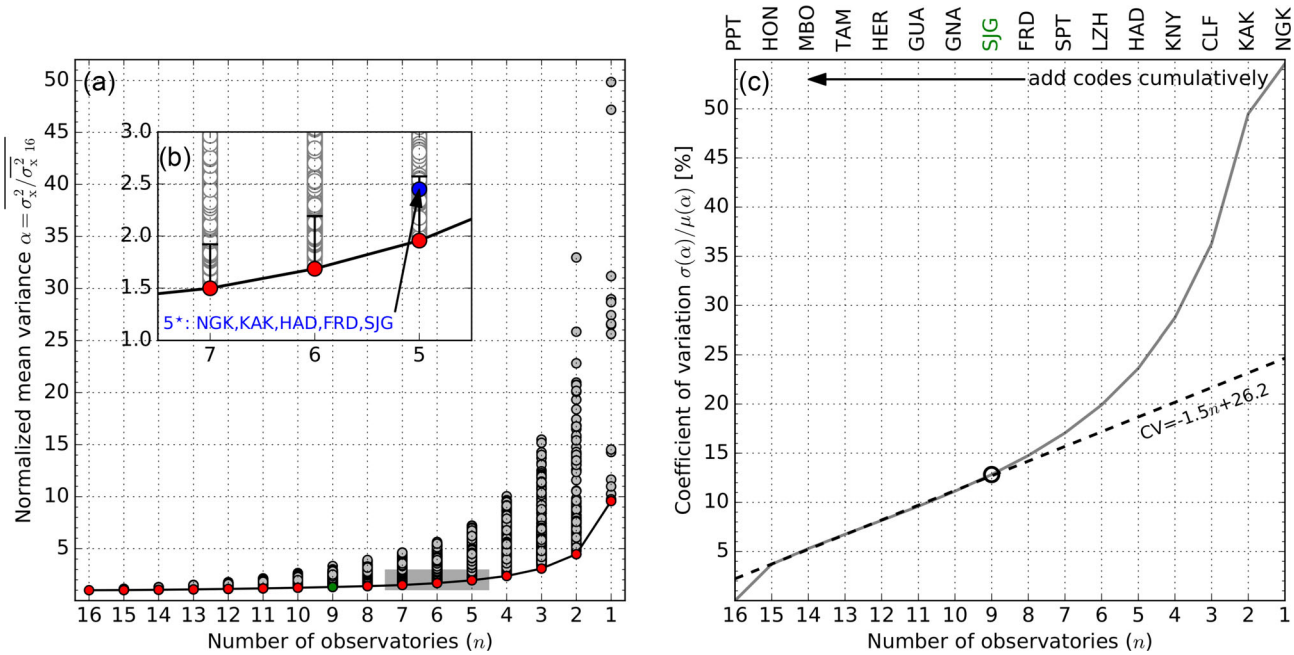

Figure 7. (a) Mean posterior variance (α) during 1960–2010 for all combinations of a particular number of observatories (grey circles) ranging from 16 to one. The black line connects station sets with minimum α for each set size ('optimum sets', red circles). The green circle marks the chosen reference set. (b) Blow-up of shaded area in panel (a). The final AMC set (5*, blue circle) falls below the 10th percentile (black horizontal bar) of the corresponding α distribution. (c) Coefficient of variation (CV) for the α distributions (grey line) and linear fit to $n = 9,\ldots,15$ observatories (dashed line). The optimum set size is fixed at $n = 9$ (black circle). IAGA codes at the top indicate which n observatories (from right to left) form the optimum sets.

5.1 AMC absolute level

The excellent agreement of signal amplitudes between AMC and the GRIMM-3.2 estimate (Fig. 6a) is not conclusive given the fact that this model was used to free our crustal biases from the average magnetospheric field (Section 3.1). However, the ∼13 nT amplitude of this field (Lühr & Maus 2010, Section 1) is adequately met by the average offset between AMC and RC indices of −12.2 nT (Fig. 6a). Furthermore, this offset is in the range of recently reported offsets amounting to −9.1 nT needed for the RCE to match annual averages of CHAMP Z_M values (Lühr *et al.* 2017) and −10 nT needed to match the $-q_1^0$ SH coefficient of the CM5 geomagnetic model (Sabaka *et al.* 2015). The significance of both these comparisons is partially restricted by the fact that AMC includes secondary induced signals in addition to the direct external field and did not undergo any subjective quiet-time selection procedure. Yet the reasonable agreements imply that the new crustal biases enable us to determine the correct baseline for the AMC index. Lastly, it is striking that the average external signal $\overline{Z_M}(t)$ surpasses the AMC index only in periods when vector satellite data is available (Section 4.1). This suggests that COV-OBS might overweight this data with respect to ground measurements, leading to an underestimation of uncertainties (see also Fig. 2). Obviously, this effect is especially strong since the beginning of the 20th century.

5.2 Observatory selection

The selection of the observatories in the reference set is based on the finding that the information extracted from different observatory measurements is redundant (see Fig. 5, top). Deviating AMC results for different observatory sets consequently arise from the input variance only and are manifest in the AMC variance (Fig. 6). Consequently the reference set should

(i) minimize the average variance over the period 1960–2010;
(ii) maximize the robustness against observatory replacement;
(iii) minimize computational complexity.

To address requirement (i), we calculated the AMC variance ($\sigma_x(q_1^0)^2$, eq. 9) for all possible combinations of candidate observatories, normalized by the average AMC variance from all these 16 stations, and averaged over the time span 1960–2010 (α). Picking the observatories associated with the minimum α ('optimum set') for each set size leads to a characteristic relation describing the most efficient reduction of index variance with data increase (Fig. 7a). Although not imposed a priori, the optimum sets are generated by cumulatively adding the observatories in a specific order starting with NGK (Fig. 7c, top). Regarding requirement (ii), we then calculated the coefficient of variation (CV) for the α distributions of each set size (Fig. 7c). CV increases linearly for sets of 15 down to nine, then rises more quickly as the observatory number decreases to one. Owing to requirement (iii), we ultimately decided for the reference set with nine stations as a compromise between a low CV and a minimum observatory number (circle in Fig. 7c).

Although the five stations in the final AMC set (Section 4.2) are not those in the optimum set of size five {NGK,KAK,CLF,KNY,HAD}, they still fall below the 10th percentile of the corresponding α distribution (Fig. 7b). This means that they sufficiently, yet not optimally, reduce the index variance during 1960–2010 while being as robust as possible against observatory drop outs during 1900–2010.

5.3 AMC application

We now turn to a demonstration of AMC index performance regarding the removal of external field signal from observatory data. Fig. 8 shows SV in the local southward component (grey) because we expect the strongest regular external field influence in this direction. SV is calculated from first differences of OAMs measured

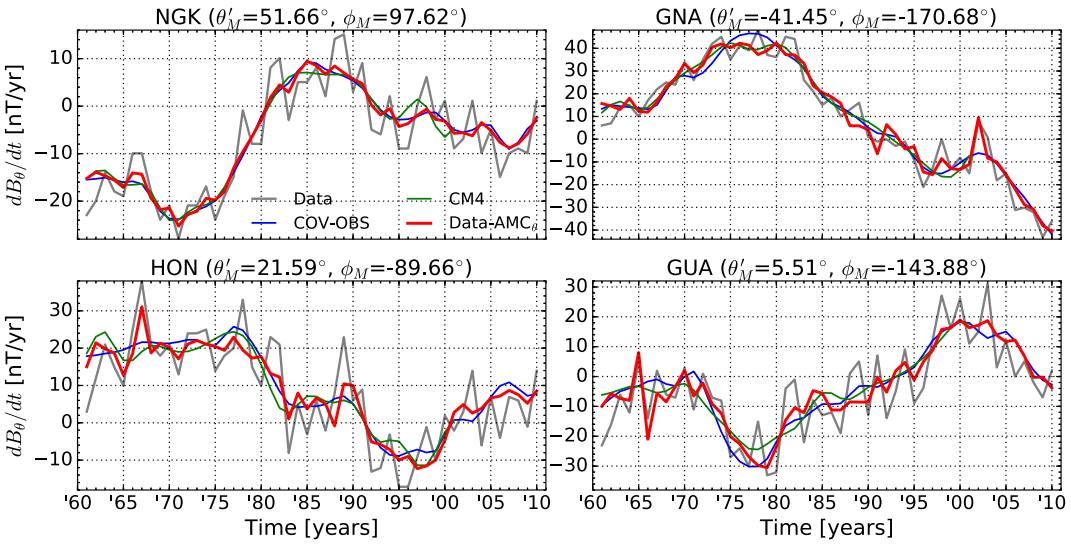

Figure 8. Comparison between SV in B_θ components (south, geocentric seu_c) from observatory measurements (grey) and AMC-corrected measurements (red) compared to modelled SV from COV-OBS (blue) and CM4 (green). The AMC index was decomposed into its vector components according to the observatory locations. These are given here in geomagnetic coordinates (*mag*).

at four locations. This is compared to modelled SV from COV-OBS (blue) and CM4 (green). The final AMC index is decomposed into its vector components (Section 3.3) and the AMC$_\theta$ time series is subtracted from the observatory measurements prior to the calculation of corrected first differences (red). In general this reduces the short-term variability of the measured SV time series so that the corrected curves display less variability than the originals, but greater variability than the smoothed global model results. This allows the identification of times at which the models might suffer locally from an incomplete separation between internal and large-scale external field components. For instance, CM4 seems to show some external field leakage around the NGK location during 1995–2001, while COV-OBS might be affected by a similar effect around GNA during 1975–1980. The latter also seems to be the case for the region around HON.

The corrected SV time series are of particular interest when trying to identify the typical 'V'-shaped signature of geomagnetic jerks. This is often done on the basis of monthly SV as in Brown *et al.* (2013) who use a method developed by Wardinski & Holme (2011) to remove external signal from the SV measurements. This signal is approximated by the SV residual between observatory data (a popular choice is NGK) and an internal magnetic field model. Compared to this procedure the application of the AMC index with improved time resolution would be less labour-intensive and more easily applicable regarding a worldwide use.

Our next aim is to increase the AMC index' temporal resolution to hourly means. This requires a dedicated removal of the ionospheric disturbance field from the observatory residuals. One approach would be to consider the magnetic field of the Sq current system as modelled by CM4 on the basis of F10.7, which reaches back to 1947. Annual reconstructions of F10.7 are available since the 17th century (Krivova *et al.* 2010). These could be sufficient to parametrize the solar cycle dependence even for the hourly index. Alternatively, Empirical Orthogonal Functions could be applied to the observatory residuals in order to extract the spatiotemporal pattern of the ionospheric disturbance field as in Shore *et al.* (2016). In either case, an AMC index with hourly resolution could readily be used by researchers investigating geomagnetic jerks as well as by global geomagnetic field modellers.

6 CONCLUSIONS

The AMC index is based on five northern hemispheric observatories (HAD, NGK, FRD, SJG, and KAK) providing annual mean data from 1900 to 2010. Compared to the Dst and RC indices it does include the average magnetospheric background signal as a consequence of recalculated crustal biases, which have systematically larger northward components than previously published values. The average offset of −12.2 nT from the RC index during 1997–2010 seems plausible when compared to other studies indicating that the intensity of the near-Earth magnetospheric field is represented correctly. Index uncertainties originate from those in the COV-OBS main field model, that can be relatively large and globally heterogeneous during the observatory era but decrease and converge notably in years with vector satellite data. At such times we suppose that COV-OBS systematically underestimates uncertainties. The final observatory combination is chosen because it provides a reasonably low average AMC variance while being robust against station replacements in case of data gaps or observatory drop outs. The preference of clustered stations over a globally uniform distribution is an interesting result in view of the signal's large-scale character. We plan to investigate this matter further when we upgrade the temporal resolution of the AMC index to hourly means in order to meet current demands for SV studies and geomagnetic field modelling.

ACKNOWLEDGEMENTS

We sincerely thank Julien Baerenzung for his advice particularly regarding the implementation of the inversion scheme and the interpretation of the results. We also thank the institutions that operate the geomagnetic observatories and host geomagnetic field models and activity indices. Special thanks go to Vincent Lesur for sharing a version of GRIMM including external sources. We appreciate the constructive comments from two anonymous reviewers, that helped to improve the manuscript.

FUNDING

This study is funded by the Priority Program 1788 'Dynamic Earth' of the German Research Foundation under grant KO2870/6-1.

REFERENCES

Bock, R., 1950. *Ergebnisse der Beobachtungen am Adolf-Schmidt-Observatorium für Erdmagnetismus in Niemegk in den Jahren 1932 und 1933,* Akademie Verlag, p. 26.

Brown, W.J., Mound, J.E. & Livermore, P.W., 2013. Jerks abound: An analysis of geomagnetic observatory data from 1957 to 2008, *Phys. Earth planet. Inter.,* **223,** 62–76.

Daglis, I.A., Thorne, R.M., Baumjohann, W. & Orsini, S., 1999. The terrestrial ring current: origin, formation, and decay, *Rev. Geophys.,* **37**(4), 407–438.

Finlay, C.C., Olsen, N., Kotsiaros, S., Gillet, N. & Tøffner-Clausen, L., 2016. Recent geomagnetic secular variation from Swarm and ground observatories as estimated in the CHAOS-6 geomagnetic field model, *Earth Planets Space,* **68**(1), 1–18.

Gannon, J.L. & Love, J.J., 2011. USGS 1-min Dst index, *J. Atmos. Sol.-Terr. Phys.,* **73**(2–3), 323–334.

Gelman, A., Carlin, J.B., Stern, H.S., Dunson, D.B., Vehtari, A. & Rubin, D.B., 2014. Fundamentals of Bayesian inference, in *Bayesian Data Analysis,* pp. 1–134, eds Dominici, F., Faraway, J. J., Tanner, M. & Zidek, J., CRC Press.

Gillet, N., Jault, D., Finlay, C.C. & Olsen, N., 2013. Stochastic modeling of the Earth's magnetic field: inversion for covariances over the observatory era, *Geochem. Geophys. Geosyst.,* **14**(4), 766–786.

Gubbins, D. & Bloxham, J., 1985. Geomagnetic field analysis–3. Magnetic fields on the core–mantle boundary, *Geophys. J. R. astr. Soc.,* **80**(3), 695–713.

Hapgood, M.A., 1992. Space physics coordinate transformations: a user guide, *Planet. Space Sci.,* **40**(5), 711–717.

Jackson, A., Jonkers, A.R.T. & Walker, M.R., 2000. Four centuries of geomagnetic secular variation from historical records, *Phil. Trans. R. Soc. A,* **358**(1768), 957–990.

Karinen, A. & Mursula, K., 2005. A new reconstruction of the Dst index for 1932-2002, *Ann. Geophys.,* **23**(2), 475–485.

Korte, M. & Lesur, V., 2012. Repeat station data compared to a global geomagnetic field model, *Ann. Geophys.,* **55**(6), 1101–1111.

Krivova, N.A., Vieira, L. E.A. & Solanki, S.K., 2010. Reconstruction of solar spectral irradiance since the maunder minimum, *J. geophys. Res.,* **115**(A12112), 1–11.

Kunagu, P., Balasis, G., Lesur, V., Chandrasekhar, E. & Papadimitriou, C., 2013. Wavelet characterization of external magnetic sources as observed by CHAMP satellite: evidence for unmodelled signals in geomagnetic field models, *Geophys. J. Int.,* **192**(3), 946–950.

Langel, R.A. & Estes, R.H., 1985a. Large-scale, near-field magnetic fields from external sources and the corresponding induced internal field, *J. geophys. Res.,* **90**(B3), 2487–2494.

Langel, R.A. & Estes, R.H., 1985b. The near-Earth magnetic field at 1980 determined from Magsat data, *J. geophys. Res.,* **90**(B3), 2495–2509.

Langel, R.A., Mead, G.D. & Estes, R.H., 1982. Some new methods in geomagnetic field modeling applied to the 1960-1980 epoch, *J. Geomagn. Geoelectr.,* **34**(6), 327–349.

Lesur, V., Rother, M., Wardinski, I., Schachtschneider, R., Hamoudi, M. & Chambodut, A., 2015. Parent magnetic field models for the IGRF-12 GFZ-candidates, *Earth Planets Space,* **67**(1), 87–102.

Lühr, H. & Maus, S., 2010. Solar cycle dependence of quiet-time magnetospheric currents and a model of their near-Earth magnetic fields, *Earth Planets Space,* **62**(10), 843–848.

Lühr, H., Xiong, C., Olsen, N. & Le, G., 2017. Near-Earth magnetic field effects of large-scale magnetospheric currents, *Space Sci. Rev.,* **206,** 521–545.

Macmillan, S. & Olsen, N., 2013. Observatory data and the Swarm mission, *Earth Planets Space,* **65**(11), 1355–1362.

Mandea, M. & Langlais, B., 2002. Observatory crustal magnetic biases during MAGSAT and Ørsted satellite missions, *Geophys. Res. Lett.,* **29**(15), ORS 4–1–ORS 4–4.

Maus, S. & Weidelt, P., 2004. Separating the magnetospheric disturbance magnetic field into external and transient internal contributions using a 1D conductivity model of the Earth, *Geophys. Res. Lett.,* **31**(12), 1–4.

Maus, S., Manoj, C., Rauberg, J., Michaelis, I. & Lühr, H., 2010. NOAA/NGDC candidate models for the 11th generation International Geomagnetic Reference Field and the concurrent release of the 6th generation POMME magnetic model, *Earth Planets Space,* **62**(10), 729–735.

Meyer, B., Saltus, R. & Chulliat, A., 2017. *EMAG2: Earth Magnetic Anomaly Grid (2-arc-minute resolution) Version 3*. National Centers for Environmental Information, NOAA. Model, last accessed 11 September 2017.

Mursula, K. & Karinen, A., 2005. Explaining and correcting the excessive semiannual variation in the Dst index, *Geophys. Res. Lett.,* **32**(14), 1–4.

Mursula, K., Holappa, L. & Karinen, A., 2011. Uneven weighting of stations in the Dst index, *J. Atmos. Sol.-Terr. Phys.,* **73**(2-3), 316–322.

Olsen, N., Sabaka, T.J. & Lowes, F., 2005. New parameterization of external and induced fields in geomagnetic field modeling, and a candidate model for IGRF 2005, *Earth Planets Space,* **57**(12), 1141–1149.

Olsen, N., Glassmeier, K.-H. & Jia, X., 2010. Separation of the magnetic field into external and internal parts, *Space Sci. Rev.,* **152**(1), 135–157.

Olsen, N., Lühr, H., Finlay, C.C., Sabaka, T.J., Michaelis, I., Rauberg, J. & Tøffner-Clausen, L., 2014. The CHAOS-4 geomagnetic field model, *Geophys. J. Int.,* **197**(2), 815–827.

Olsen, N. *et al.*, 2015. The Swarm Initial Field Model for the 2014 geomagnetic field, *Geophys. Res. Lett.,* **42**(4), 1092–1098.

Sabaka, T.J., Olsen, N. & Purucker, M.E., 2004. Extending comprehensive models of the Earth's magnetic field with Ørsted and CHAMP data, *Geophys. J. Int.,* **159**(2), 521–547.

Sabaka, T.J., Olsen, N., Tyler, R.H. & Kuvshinov, A., 2015. CM5, a pre-Swarm comprehensive geomagnetic field model derived from over 12 yr of CHAMP, Ørsted, SAC-C and observatory data, *Geophys. J. Int.,* **200**(3), 1596–1626.

Schmidt, A., 1917. Erdmagnetismus, in *Encyklopädie der mathematischen Wissenschaften mit Einschluss ihrer Anwendungen,* pp. 266–396, eds Furtwängler, P.H. & Wiechert, E. B. G. Teubner Verlag.

Shore, R.M., Whaler, K.A., Macmillan, S., Beggan, C., Velímský, J. & Olsen, N., 2016. Decadal period external magnetic field variations determined via eigenanalysis, *J. geophys. Res.,* **121**(6), 5172–5184.

Sugiura, M., 1964. Hourly values of equatorial Dst for the IGY, *Ann. Int. Geophys. Year,* **35,** 4–45.

Thébault, E., Hemant, K., Hulot, G. & Olsen, N., 2009. On the geographical distribution of induced time-varying crustal magnetic fields, *Geophys. Res. Lett.,* **36**(1), 1–5.

Thébault, E. *et al.*, 2015. International geomagnetic reference field: the 12th generation, *Earth Planets Space,* **67**(79), 1–19.

Thomson, A.W.P. & Lesur, V., 2007. An improved geomagnetic data selection algorithm for global geomagnetic field modelling, *Geophys. J. Int.,* **169**(3), 951–963.

Verbanac, G., Lühr, H., Rother, M., Korte, M. & Mandea, M., 2007. Contributions of the external field to the observatory annual means and a proposal for their corrections, *Earth Planets Space,* **59**(4), 251–257.

Verbanac, G., Mandea, M., Bandić, M. & Subašić, S., 2015. Magnetic observatories: biases over CHAMP satellite mission, *J. Geophys. Res.,* **6**(2), 775–781.

Wardinski, I. & Holme, R., 2011. Signal from noise in geomagnetic field modelling: denoising data for secular variation studies, *Geophys. J. Int.,* **185**(2), 653–662.

Wolf, R.A. & McPherron, R.L., 1995. Magnetospheric Configuration & Magnetospheric Dynamics, in *Introduction to Space Physics,* pp. 288–329 & 400–458, eds Kivelson, M.G. & Russell, C. T., Cambridge Univ. Press.

SUPPORTING INFORMATION

Supplementary data are available at *GJIRAS* online.

AMC.docx

Please note: Oxford University Press is not responsible for the content or functionality of any supporting materials supplied by the authors. Any queries (other than missing material) should be directed to the corresponding author for the paper.

APPENDIX A: COORDINATE SYSTEMS

Table A1 summarizes the used coordinate systems and the nomenclature of the associated components in the position and field vectors.

Table A1. Nomenclature of field and position vector components in the different coordinate systems used. *ned* abbreviates *n*orth, *e*ast, *d*own and *seu* abbreviates *s*outh, *e*ast, *u*p. Note that $\dot{X} = -B_\theta$, $Y = \dot{Y} = B_\phi$ and $\dot{Z} = -B_r$. Latitudes are labelled θ' while colatitudes are labelled θ.

	Position vector			Field vector		
System	Pos.1	Pos. 2	Pos. 3	Field 1	Field 2	Field 3
Spheroidal ned_d	θ'_d	ϕ	h	X	Y	Z
Spherical ned_c	θ'_c	ϕ	r	$\dot{X}$	$\dot{Y}$	$\dot{Z}$
Spherical seu_c	θ_c	ϕ	r	B_θ	B_ϕ	B_r
Cartesian GEO	x_G	y_G	z_G	X_G	Y_G	Z_G
Cartesian MAG	x_M	y_M	z_M	X_M	Y_M	Z_M
Spherical *mag*	θ_M	ϕ_M	r	$B_{\theta,M}$	$B_{\phi,M}$	$B_{r,M}$

APPENDIX B: DATA SOURCES

(1) Data:

(i) OAMs – BGS (http://www.geomag.bgs.ac.uk/data_service/data/annual_means.shtml), last accessed 10 September 2017.

(2) Activity indicators:

(i) Dst – NOAA (ftp://ftp.ngdc.noaa.gov/STP/GEOMAGNETIC_DATA/INDICES/EST_IST), last accessed 10 September 2017.
(ii) Dcx – University of Oulu, Finland (http://dcx.oulu.fi/dldatadefinite.php), last accessed 10 September 2017.
(iii) Ap – GFZ Potsdam via WDC Kyoto (http://wdc.kugi.kyoto-u.ac.jp/kp/index.html), last accessed 10 September 2017.
(iv) RC – DTU Space (http://www.spacecenter.dk/files/magnetic-models/RC/), version from 12/06/17, last accessed 10 September 2017.
(v) F10.7 – NOAA (ftp://ftp.ngdc.noaa.gov/STP/space-weather/solar-data/solar-features/solar-radio/noontime-flux/penticton/penticton_absolute/listings), 'Series D Flux', last accessed 10 September 2017.
(vi) Total sunspot number – WDC-SILSO, Royal Observatory of Belgium, Brussels (URL) (http://www.sidc.be/silso/datafiles), last accessed 10 September 2017.

(3) Models:

(i) COV-OBS – DTU Space (http://www.spacecenter.dk/files/magnetic-models/COV-OBS/), last accessed 10 September 2017.
(ii) GRIMM series – GFZ Potsdam (http://www.gfz-potsdam.de/en/section/earths-magnetic-field/topics/field-models/grimm-x/), up to version 3.0, last accessed 10 September 2017.
(iii) CM4 – NASA (https://denali.gsfc.nasa.gov/geomag.html), not available anymore, last accessed 10 September 2017.
(iv) POMME-8 – CIRES (http://geomag.org/models/pomme8.html), last accessed 10 September 2017.

APPENDIX C: OBSERVATORY INFORMATION

Table C1 lists observatory locations in geodetic and geomagnetic coordinates as well as our recalculated crustal biases.

Table C1. Locations of candidate observatories and corresponding crustal biases. Locations in geomagnetic coordinates were calculated for mid-2010 by linear interpolation between coefficients from IGRF-12 (Thébault *et al.* 2015). OAMs for 1997–2010 were checked against annual means from OHMs revised by Macmillan & Olsen (2013). Three OAMs were replaced by these corrected data (KNY *X*&*Y* at 2003.5 and ESA *X* at 2001.5). Observatories used to derive the AMC index have bold IAGA codes.

	Geodetic coord. (ned_d)			Geomagnetic coord. (mag)			Crustal bias (ned_d)		
Code	lat (°) θ'_d	lon (°) ϕ	alt (km) h	lat (°) θ'_M	lon (°) ϕ_M	rad (km) r - 6371	Xb (nT)	Yb (nT)	Zb (nT)
HAD	51.0	− 4.48	0.095	53.58	80.15	− 5.64	− 38.89	14.1	69.32
NGK	52.07	12.68	0.078	51.66	97.62	− 6.05	− 18.28	− 3.1	− 84.02
CLF	48.03	2.26	0.145	49.56	85.72	− 4.49	− 65.11	− 15.79	101.0
FRD	38.21	− 77.37	0.069	47.93	− 6.02	− 0.93	73.42	− 50.88	116.84
SPT	39.55	− 4.35	0.922	42.45	76.13	− 0.57	9.86	9.09	− 30.43
SJG	18.12	− 66.15	0.424	27.9	6.57	5.51	− 47.27	135.39	127.52
KAK	36.23	140.19	0.036	27.49	− 150.73	− 0.26	8.02	12.01	− 100.3
LZH	36.09	103.85	1.56	25.97	176.48	1.32	23.05	0.43	− 103.64
TAM	22.79	5.53	1.373	24.4	82.06	5.32	59.83	− 220.96	− 50.2
KNY	31.42	130.88	0.107	22.03	− 158.76	1.47	5.91	53.01	− 49.88
HON	21.32	− 158.0	0.004	21.59	− 89.66	4.33	− 160.34	84.97	− 331.6
MBO	14.38	− 16.97	0.007	19.78	57.83	5.84	125.59	35.24	66.69
GUA	13.59	144.87	0.14	5.51	− 143.88	6.11	135.82	76.39	41.64
PPT	− 17.57	− 149.57	0.357	− 15.03	− 74.5	5.56	− 894.97	− 1034.71	− 390.18
HER	− 34.43	19.23	0.026	− 33.91	84.72	0.37	30.36	9.05	31.25
GNA	− 31.78	115.95	0.060	− 41.45	− 170.68	1.30	− 13.36	− 100.61	115.75

APPENDIX D: ADDITIONAL FIGURES

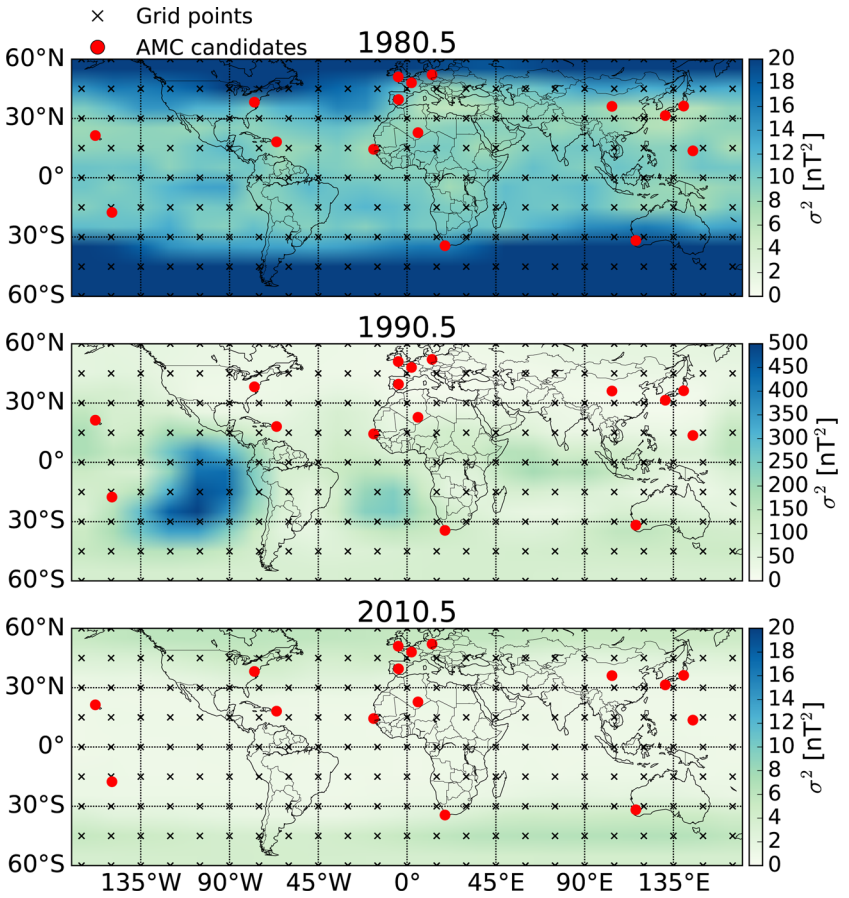

Figure D1. Interpolated main field variances σ^2 on a 15°lat/15°lon grid (black crosses) from COV-OBS ensemble (100 members). For each location variances of all three vector components *X*, *Y* & *Z* were calculated and then averaged. Red dots indicate the locations of the 16 AMC candidate observatories. The chosen times 1980.5, 1990.5 and 2010.5 correspond to those indicated by black vertical lines in Fig. 6(a). Note the different scale of the colour bars for 1980.5/2010.5 and 1990.5.

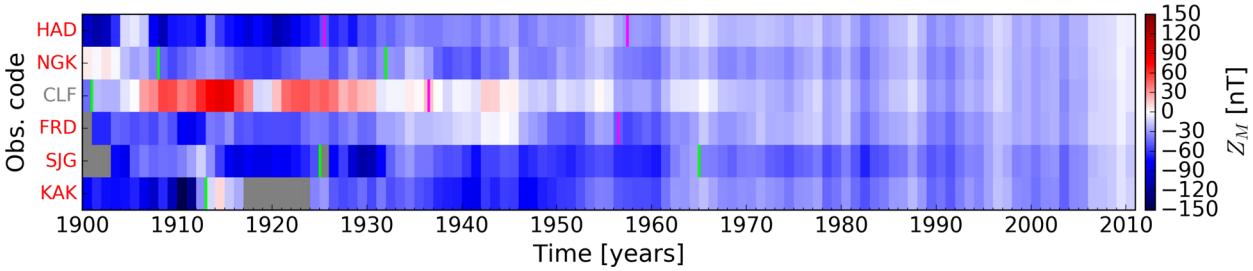

Figure D2. Observatory residuals Z_M (north, geomagnetic MAG) from six observatories spanning 1900–2010 sorted by geomagnetic latitude from north (top) to south (bottom). Red IAGA codes indicate observatories chosen for the AMC data set. Vertical bars indicate relocations of the observatories that either offer an overlap of OAMs (magenta) or not (green). The consecutive IAGA codes are GRW→ABN→**HAD**, POT→SED→**NGK**, PSM→VLJ→**CLF**, CLH→**FRD**, VQS→SJG1→**SJG2**, TOK→**KAK**.